



HAL
open science

SPH modeling of fluid-solid interaction for dynamic failure analysis of fluid-filled thin shells

Fabien Caleyron, Alain Combescure, Vincent Faucher, S. Potapov

► **To cite this version:**

Fabien Caleyron, Alain Combescure, Vincent Faucher, S. Potapov. SPH modeling of fluid-solid interaction for dynamic failure analysis of fluid-filled thin shells. *Journal of Fluids and Structures*, 2013, 39, pp.126-153. hal-00819622

HAL Id: hal-00819622

<https://hal.science/hal-00819622>

Submitted on 2 May 2013

HAL is a multi-disciplinary open access archive for the deposit and dissemination of scientific research documents, whether they are published or not. The documents may come from teaching and research institutions in France or abroad, or from public or private research centers.

L'archive ouverte pluridisciplinaire **HAL**, est destinée au dépôt et à la diffusion de documents scientifiques de niveau recherche, publiés ou non, émanant des établissements d'enseignement et de recherche français ou étrangers, des laboratoires publics ou privés.

SPH modeling of fluid-solid interaction for dynamic failure analysis of fluid-filled thin shells

F. Caleyron^{a,b}, A. Combescure^{a,*}, V. Faucher^{b,c}, S. Potapov^b

^a*Université de Lyon, CNRS, INSA-Lyon, LaMCoS UMR 5259, F-69621, France*

^b*LaMSID UMR EDF-CNRS-CEA 2832*

^c*CEA DEN, DM2S, Laboratoire d'Etude de Dynamique, F-91191 Gif-sur-Yvette, France*

Abstract

This work concerns the prediction of failure of a fluid-filled tank under impact loading, including the resulting fluid leakage. A water-filled steel cylinder associated with a piston is impacted by a mass falling at a prescribed velocity. The cylinder is closed at its base by an aluminum plate whose characteristics are allowed to vary. The impact on the piston creates a pressure wave in the fluid which is responsible for the deformation of the plate and, possibly, the propagation of cracks. The structural part of the problem is modeled using Mindlin-Reissner Finite Elements (FE) and Smoothed Particles Hydrodynamics (SPH) shells. The modeling of the fluid is also based on an SPH formulation. The problem involves significant Fluid-Structure Interactions (FSI) which are handled through a master-slave-based method and the pinballs method. Numerical results are compared to experimental data.

Keywords: SPH, fluid-structure interaction, impact, failure

*. Corresponding author : Tel : +33 4 72 43 64 26, Fax : +33 4 78 89 09 80
Email address: alain.combescure@insa-lyon.fr (A. Combescure)

1. Introduction

The recent increase in terrorist threats has led to an intensification of research efforts in order to protect citizens and industrial installations. Numerous scenarios, such as the fall of a commercial aircraft on a civil engineering structure, must be envisaged.

In this context, the analysis of the fracture and leakage of a thin fluid-filled structure, such as an aircraft's fuel tank, is an especially important undertaking. This is a complex problem which involves highly nonlinear phenomena both in the fluid (sloshing, splashing, shock waves, cavitation) and in the structure (large strains, damage, cracking, dynamic fracture). Moreover, the interface between the two media can undergo drastic changes during the process, for example in the case of significant movements of the free surface of the fluid or the rupture of the tank.

The simulation of this type of problem is a real scientific challenge for which research is still ongoing. The literature recounts different approaches which are briefly summarized below.

Some authors, such as Timm in (Timm, 2003), use the classical Lagrangian formulation of the FEM. However, this approach has shortcomings : in particular, highly distorted meshes lead to numerical errors and a decrease in time steps which affect the effectiveness and efficiency of the method. These problems can sometimes be circumvented through erosion of the distorted elements, but this approach precludes the conservation of the mass and energy of the model throughout the calculation, except if the eroded elements are replaced by debris as in (Sauer, 2010).

26 Sometimes, Eulerian approaches are also used, e.g. in (Anderson et al.,
27 1999), especially to study the fluid part of the problem. Indeed, in this case,
28 the mesh does not vary with time and, thus, it remains valid regardless of
29 the strains undergone by the material. However, in this context, the study of
30 the structure is difficult, particularly if it is thin and ruptures. Therefore, the
31 Eulerian fluid model is sometimes coupled with a FE model of the structure.

32 An intermediate approach consists in using an Arbitrary Lagrangian-
33 Eulerian (ALE) model, which enables Lagrangian calculations to be carried
34 out while leaving the possibility for the mesh to evolve independently of the
35 medium in order to avoid, for example, excessive distortions. The ALE model
36 can be used to represent the whole problem or the fluid alone (Varas
37 et al., 2009b) while the fluid tank and the impactor are modeled using the
38 FEM.

39 Finally, an interesting approach for this class of problems consists in using
40 meshless methods. Indeed, these methods enable large strains and the intro-
41 duction of discontinuities such as cracks to be handled naturally. One can
42 cite the works of Maurel *et al.* (Maurel et al., 2009; Potapov et al., 2009)
43 and Caleyron *et al.* (Caleyron et al., 2011), who proposed a model based
44 entirely on the SPH method for the analysis of tanks under impact. Rab-
45 zuk *et al.* also proposed models based on the Element-Free Galerkin (EFG)
46 meshless method for the resolution of this type of problem (Rabczuk et al.,
47 2007, 2009). In some cases, the meshless model is used only for the fluid part
48 of the problem (Varas et al., 2009b), sometimes even in an adaptive way as
49 a function of the progression of the projectile into the fluid (Sauer, 2010).

50 In this paper, an SPH model is used for the fluid for the reasons mentio-

51 ned previously. The tank is modeled classically using the FEM, except in the
52 zones subjected to fracture. In this case, a specific SPH shell model presented
53 in (Maurel et al., 2009; Potapov et al., 2009; Caleyron et al., 2011) is used
54 locally.

55

56 The availability of reliable experimental data is also important in order to
57 evaluate the performance of the numerical models thus defined. The experi-
58 ments developed for that purpose must be simple, well-designed and properly
59 instrumented as well as representative of the phenomenon being studied.

60 The literature abounds with experimental studies concerning the “hydro-
61 dynamic ram” (HRAM) phenomenon which occurs during high-speed impact
62 on a fluid-filled tank (Disimile et al., 2009; Varas et al., 2009a; Freitas et al.,
63 1996, 1997). In this case, the projectile transfers its kinetic energy to the
64 structure via the fluid, which, thus, can lead to the complete failure of the
65 tank. However, most of the studies focus mainly on the behavior of the fluid
66 (shock waves, cavitation) while the strains in the structure remain small
67 outside of the perforation zone.

68 Far fewer experimental works focus precisely on the fracture of the struc-
69 ture. One can cite the works by Timm (Timm, 2003) on the impact of a
70 bullet onto an empty or water-filled cylinder for various impact velocities
71 and cylinder dimensions. The author showed that for sufficiently high inco-
72 ming velocities the impact results in the propagation of a longitudinal crack
73 on the impacted side of the tank. Rabczuk *et al.* compared these experi-
74 mental data with results from simulations using meshless models (Rabczuk
75 et al., 2007, 2009). In (Sauer, 2010), Sauer studied the fragmentation of a

76 cylinder impacted by a projectile. The cylinder was filled with water and,
77 in some of the cases, presented precracks. The experimental data (residual
78 velocity of the projectile, fracture mode, distribution of the fragments) were
79 also compared to the results of simulations using SPH and FE models.

80 One can also mention interesting experiments involving the fracture of
81 tubes (Chao and Shepherd, 2005) or tanks (Keesecker et al., 2003) under
82 internal pressure. The corresponding simulations have been reported, for
83 example, in (Rabczuk et al., 2007, 2009).

84 In this context, this paper presents an original experiment which is re-
85 presentative of a tank subjected to an impact. This enables us to study the
86 behavior of a plate interacting with a fluid while controlling the phenomena
87 involved : simple water flow, large strains, cracking or even the complete
88 rupture of the tank. Some of the experimental data were already presented
89 in (Potapov et al., 2009). This paper completes the previous publication by
90 providing the full experimental results as well as the corresponding simula-
91 tions.

92
93 The paper is divided into four sections. The first section presents the ex-
94 perimental setup. In the second section, the results are examined in detail and
95 interpreted in order to emphasize the phenomena involved in the experiment.
96 The third section is devoted to the description of the associated numerical
97 model. In the last section, the results given by the model are compared to
98 the experimental data.

99 2. Presentation of the tests

100 The objective of the test campaign was to provide an experimental setup
101 which would be simple, yet representative of an impact on a fluid-filled tank.
102 Thus, the principle of the experiment was simple : a cylinder, closed by a
103 metal plate which constituted the zone of interest, was filled with water,
104 then fitted with a piston which was impacted by a mass. The impact created
105 a pressure shock in the water, leading to a deformation of the specimen
106 followed by the propagation of a crack and, ultimately, the leakage of the
107 water contained in the piston. The experimental campaign was carried out at
108 ONERA in Lille by J. Fabis in 2006. This section describes the experimental
109 setup, the characteristics of the specimens used, the scenarios of the tests
110 and the measurement system.

111 2.1. The experimental setup

112 The experimental setup is shown in Figure 1. It consisted essentially of
113 a thick cylinder ($e_{cyl} = 15 \text{ mm}$, $D_{cyl} = 80 \text{ mm}$) associated with a piston.
114 Both elements were made of steel (APX Z15 CN 17.03). The cylinder was
115 closed at the bottom by a plate which constituted the zone of interest of the
116 experiment and whose characteristics were allowed to vary depending on the
117 tests : different thicknesses, presence of a hole or precracks in order to observe
118 different types of behavior. These specimens were made of aluminum (AU4G
119 2024 T351) so they could deform more easily than the cylinder. The cylinder
120 was filled with water to form a column of height $H = (205 - e_p) \text{ mm}$, e_p being
121 the thickness of the specimen. The pressure shock in the water was created
122 by the fall of a mass $M = 245 \text{ kg}$ onto the piston. In order to do that, we

123 used the drop tower at ONERA in Lille and attached the mass to a carriage
124 guided by a system of rails (see Figure 2). Two impact velocities, $V_1 = 2 \text{ m/s}$
125 and $V_2 = 5 \text{ m/s}$, were considered. These were obtained by selecting the pro-
126 per carriage release height H_l using the formula $H_l = V^2/2g$. The drop tower
127 was installed on an 80 t foundation which enabled the crash zone to be un-
128 coupled from the rest of the structure. The experimental setup allowed good
129 monitoring of the experimental parameters : mass, impact velocity, angle of
130 incidence, resonance frequencies, etc. Moreover, special care was given to the
131 setting of the boundary conditions of the aluminum specimen, as explained
132 in the following section.

133

134 *Note : aluminum grade AU4G 2024 T351 was chosen because its behavior*
135 *is hardly affected by the strain rate, thus enabling a simple constitutive rela-*
136 *tion to be used in the simulations.*

137 2.2. Characteristics of the specimens

138 The aluminum specimens had various characteristics which enabled us to
139 control the phenomena involved in the experiment (water flow, deformation of
140 the bottom, cracking or fracture). The following configurations were tested :

- 141 • a circular hole with a diameter $d = 14 \text{ mm}$ or $d = 20 \text{ mm}$;
- 142 • a U-shaped precrack of length $3 \times 20 \text{ mm}$;
- 143 • two 30 mm precracks forming an X ;
- 144 • no hole or precrack ;
- 145 • a circular hole with a diameter $d = 14 \text{ mm}$ and two diametrically
146 opposed 3 mm precracks ;

147 • an I-shaped precrack of length 20 *mm*.

148

149 The thickness of the part of the specimen in contact with the fluid was
150 also allowed to vary. The plates were manufactured from a $200 \times 200 \times 25$ *mm*
151 aluminum block whose center part, of diameter $D_{cyl} = 80$ *mm*, was spot-faced
152 in order to obtain three different thicknesses : $e_p = 25$ *mm* (no spot-facing,
153 thick specimen), $e_p = 2$ *mm* (thin specimen) and $e_p = 1$ *mm* (ultra-thin spe-
154 cimen). The different tests are listed in Table 4 along with the characteristics
155 of the corresponding specimen. Examples of specimens in their initial state
156 are shown in Figure 3.

157

158

159 As can be seen in Figure 3, the specimens were fitted with 12 circularly ar-
160 ranged holes to provide the connection with the cylinder. Additionally, they
161 were fastened to the visualization space by means of 8 additional screws.
162 Figure 4(a) represents a specimen attached to the experimental device ac-
163 cording to the principle shown in Figure 4(b).

164 *2.3. The testing procedure*

165 The exact same procedure was followed for all the tests in order to achieve
166 maximum reproducibility :

- 167 • the specimen was fastened to the end of the cylinder ;
- 168 • the holes were sealed with adhesive tape ;
- 169 • the cylinder was filled with water with no residual bubbles ;
- 170 • contact between the carriage and the piston was established and the
171 height measurement was set to zero ;

- 172 • the displacement sensor was verified ;
- 173 • the carriage was raised to the desired release height ;
- 174 • the spotlights were turned on behind a black screen to avoid overheating
- 175 the setup ;
- 176 • the measuring bridge automatic balance was performed, the pressure
- 177 measurement reset to zero and the acquisition device and high-speed
- 178 camera were wound up ;
- 179 • the black screen was removed, the crash area cleared and the release
- 180 activated.

181 *2.4. The acquisition apparatus*

182 A data acquisition chain was used to collect a variety of information
183 precisely throughout the experiments :

- 184 • an optical displacement sensor was used to track the course of the
- 185 carriage ;
- 186 • a high-extension strain gage ($\sim 15\%$) was affixed to each specimen in a
- 187 zone which would be solicited by the pressure shock. These gages were
- 188 associated with a 75 kHz low-pass filter. The objective was to collect
- 189 the strain state and the residual plasticity state at the position of the
- 190 gage ;
- 191 • a piezoelectric pressure gage (measuring range 1,000 bar, eigenfrequency
- 192 150 kHz) was fastened to the underside of the cylinder in order to mea-
- 193 sure the evolution of the pressure at a point of the tank ;
- 194 • a high-speed, high-definition camera (4,000 images per second and
- 195 768×512 pixel resolution) was used to monitor the behavior of the
- 196 specimen and the flow. It also enabled us to estimate the velocity of

197 the water outflow from the cylinder. High-power cold-light spotlights
198 enabled the exposure time to be limited to 15 μs without heating the
199 specimens.

- 200 • a piezoelectric load sensor was placed under the specimen in the visua-
201 lization space to measure the load exerted by the water jet ;
- 202 • in order to acquire all these data synchronously, we used a multi-
203 channel analyzer equipped with acquisition cards capable of 1 million
204 samples per second.

205 **3. Analysis of the tests**

206 This section presents the results obtained for the different configurations
207 and discusses their interpretation. The tests which did not involve fracture (1
208 to 9, 10, 12 and 13) will be studied first because they give an understanding
209 of the behavior of the experimental setup. Then, the tests with fracture (11
210 and 14 to 19) will be analyzed.

211 *3.1. The tests without fracture*

212 *3.1.1. Observations*

213 Tests 1 through 9 (E14A-B-C2, E14A-B-C-D5, E20A2 and E20A5) were
214 the simplest because the bottom was thick and had a single hole. Therefore,
215 it deformed only slightly and the consequences of the impact reduced to
216 the creation of a water jet spouting out of the cylinder. The curves plotted
217 from the pressure measurements inside the cylinder for tests E14A-B-C2 and
218 E14A-B-C-D5 are shown in Figures 5 and 6.

219 These signals can be divided into two parts :

- 220 • Immediately following the impact, a pressure peak occurred and slightly
221 affected the measurement. More precisely, this peak varied between 210
222 and 277 *bars* for tests E14A-B-C-D5, and between 58 and 83 *bars* for
223 tests E14A-B-C2. This dispersion was probably due to the fact that
224 the impact triggered a vibration of all the components of the device,
225 which perturbed the measurements.
- 226 • After the impact, the flow through the hole became steady. Then, the
227 results were highly reproducible, particularly for tests E14A-B-C-D5,
228 which confirms the quality of the setup and of the measuring system.
229 For all the tests, a highly reproducible pressure decrease associated with
230 periodical variations was observed during the flow. Therefore, this de-
231 crease could not be due to measurement noise and must be attributed
232 to a physical phenomenon, a conclusion made even stronger by the care
233 with which the gages were chosen in order to eliminate measurement
234 problems (150 *kHz* resonance frequency, 75 *kHz* low-pass filter).

235

236 These periodic pressure variations for tests E14A-B-C-D5, E14A-B-C-D2,
237 E20A2 and E20A5 were related to the observation of phenomena with the
238 same frequency in the associated water jet (see Figure 8(a)). The water flow
239 was highly turbulent with a Reynolds number of about $1.e^6$. It started in the
240 form of a “mushroom”, as shown in Figure 7, when the water was expelled
241 from the cylinder ; then, once the flow became steady, the jet came to a dia-
242 meter slightly smaller than the hole and a bulb-shaped pattern was observed
243 (see Figure 8(a)). These bulbs appeared during the flow at a constant fre-
244 quency which was close to that observed for the pressure signal. At the end

245 of the flow, the bulbs disappeared and a perfectly cylindrical jet could be
246 observed briefly (see Figure 8(d)).

247 In the case of deformable specimens (such as in tests F14A2, FUA5 and
248 FUA2), a periodical signal with the same frequency was also measured by
249 the strain gage, as can be seen in the comparison of the pressure and strain
250 signals for test F14A2, in which the gage was placed at a distance $(D_{ext} + d)/4$
251 from the center of the plate (see Figure 9).

252 Finally, tests FUA2 and FUA5 presented no fracture or cracking either.
253 Indeed, the U-shaped precrack flexed under pressure and opened to let the
254 fluid escape. The opening angle of the tongue thus formed was a function of
255 the impact velocity, as shown in Figure 10.

256 The water jet presented no bulbs because it was perturbed by the incom-
257 pletely open tongue (see Figure 11).

258 However, the curves obtained from the pressure and strain gages had
259 the same characteristics as in the previous tests. Indeed, Figure 12 shows
260 the same in-phase periodical variations of the pressure and strain signals.
261 (Here, the pressure gage was placed in the tongue's bending zone, as shown
262 in Figure 3.) One can observe that in these two tests the strains reached
263 significant levels (1.8 % for FUA2 and 2.0 % for FUA5), which means that
264 plasticity was taking place at the measurement point. This is confirmed by
265 the existence of a residual opening of the tongues in Figure 10.

266 An analysis of the signals through Fourier series decomposition shows
267 that the frequency observed was about $f \sim 1600 \text{ Hz}$ for tests 1 through 9,
268 $f \sim 1000$ to 1200 Hz for test 10 and $f \sim 1300 \text{ Hz}$ for tests 12 and 13.

269 *3.1.2. Interpretations*

270 Despite the apparent simplicity of tests 1 to 13, the experimental data
271 reveal the occurrence of complex phenomena. Indeed, the pressure and strain
272 signals present in-phase periodical variations which can be compared to the
273 occurrence, at the same frequency, of bulbs in the water stream. The fre-
274 quency observed varied slightly with the geometry of the specimens (see
275 Table 5). Higher frequencies were observed in the tests associated with a
276 thick bottom.

277 The interpretation of these phenomena is not easy. The simplest explana-
278 tion would consist in attributing the periodical variations to the shock wave
279 traveling back and forth in the fluid column, but two arguments invalidate
280 that explanation. First, according to that theory, the frequency observed
281 should increase as the water level in the cylinder decreases, and not remain
282 constant as was actually observed. Second, the measured frequency should
283 be higher, of the order of $f = c/(2H) \sim 4,000 \text{ Hz}$, $c = 1,450 \text{ m/s}$ being the
284 velocity of sound in water.

285 In fact, the pattern shown in Figure 8(a) corresponds to an instability of
286 the type which develops classically in highly turbulent jets, called Plateau-
287 Rayleigh instability. For this instability to develop, the jet must first be
288 solicited. The excitation frequency controls the frequency of occurrence of
289 the patterns in the jet. In our case, it is likely that the shock solicited the
290 eigenmodes of the fluid-structure oscillator formed by the experimental setup,
291 leading to the development of bulb-shaped instabilities in the jet. Thus, the
292 frequencies observed probably correspond to an eigenmode of the assembly.
293 This is consistent with the decrease in frequency observed in the case of thin

294 specimens. A simplified model of a cylinder filled with water was studied
295 using the CASTEM software. The frequency of the first eigenmode of the
296 model was found to be approximately $f \sim 1,300 \text{ Hz}$, which confirms the
297 previous reasoning. Figure 13 shows the associated deflection and the pressure
298 isocurves in the fluid for $e_p = 1 \text{ mm}$.

299 *3.2. The tests with fracture*

300 Let us now consider tests 11 and 14 to 19. These tests involved crack
301 propagations leading, in some cases, to the complete rupture of the specimen.
302 These phenomena were combined to those described in the previous section.

303 In tests TF14A5, F14A2-5 and TFA5, the rupture of the bottom at the
304 level of the spot-facing circumference was observed. The final state of the
305 specimens is shown in Figure 14. This phenomenon, which had not been
306 anticipated at the time the specimens were designed, is due to the presence
307 of stress concentrations, particularly shear stresses, at the level of the junction
308 between the thin part and the thick bottom.

309 In the case of tests FXA2, FXA5, F14E3A5 and FE20A5, cracks propaga-
310 ted starting from the notches, as can be seen in Figure 15. However, contrary
311 to the previous cases, one can note that the bottom was not completely
312 ruptured.

313 **4. The numerical model**

314 This section presents the numerical model associated with the tests des-
315 cribed previously. Since the correct eigenfrequency of the system appears to
316 be important in order to achieve a good description of the problem, we chose

317 to represent the various elements of the assembly explicitly. The model is
318 shown in Figure 16.

319 *4.1. The structural model*

320 The cylinder was modeled using Q4GS thick shell finite elements (5 in-
321 tegration points through the thickness, selective integration) and the piston
322 was represented as a material point connected to beam elements. The car-
323 riage was represented by its complete mass $M = 245 \text{ kg}$ concentrated into a
324 material point. Depending on the case, the specimen was represented in two
325 different ways :

- 326 • In the absence of crack propagation, Q4GS finite elements were used.
- 327 • In the presence of cracks, a shell model based on the SPH meshless
328 method was used. Indeed, this model, which was presented in (Maurel
329 and Combescure, 2008; Caleyron et al., 2011), is dedicated to fracture
330 and crack propagation phenomena. A brief description will be given in
331 Section 5.4.1.

332 The constitutive relations used were simple because the behavior of AU4G
333 and APX materials can be considered to be independent of the strain rate.
334 Therefore, Von Mises' elastic-plastic laws were used. A description of the
335 parameters is given in Figure 17 and Tables 1 and 2. In the case of tests with
336 fracture, Von Mises' elastic-plastic behavior of AU4G aluminum was coupled
337 with a Lemaitre and Chaboche damage law. This coupling will be described
338 in Section 5.3.1.

339 Both the specimen and the lower part of the cylinder were built-in. We
340 also chose to fix the upper part of the cylinder radially in order to represent
341 the massive head of the piston (see Figure 4(b)).

342 Altogether, the structural model consisted of about 1,700 Q4GS elements.

343 4.2. The fluid model

344 The fluid was modeled using the SPH method. Let us briefly review the
345 equations of the model and their discretization. The fluid was assumed to
346 be :

- 347 • perfect, *i.e.* exempt from viscosity. Thus, the equilibrium equation is :

$$\frac{\partial \vec{v}}{\partial t} = -\frac{1}{\rho} \nabla p \quad (1)$$

348 where \vec{v} is the velocity vector, p the pressure, ρ the density and t the
349 time.

- 350 • weakly compressible. Thus, the continuity equation is :

$$\frac{\partial \rho}{\partial t} + \rho \nabla \cdot \vec{v} = 0 \quad (2)$$

351 The term $\partial \rho / \partial \vec{x} \cdot \vec{v}$ (where \vec{x} is the position vector) was ignored,
352 meaning that the density variations were assumed to be orthogonal to
353 the velocity vector \vec{v} . This assumption is valid for water as long as the
354 velocity remains small compared to the velocity of sound c .

- 355 • acoustic. Thus, the state equation is :

$$dp = c^2 d\rho \quad (3)$$

356 This law is valid for slightly compressible fluids such as water as long
357 as the velocity in the fluid remains small compared to the velocity of
358 sound c .

359

360 The fluid model is based on a classical SPH formulation, whose charac-
 361 teristics are the following :

- 362 • The SPH kernel W_{ij} is a B3 spline.
- 363 • The equilibrium equation is discretized as :

$$\left(\frac{\partial \vec{v}}{\partial t}\right)_i = - \sum_j m_j \left(\frac{p_i}{\rho_i^2} + \frac{p_j}{\rho_j^2}\right) \vec{\nabla} W_{ij} \quad (4)$$

364 where i is the current particle and j is one of its neighbors of mass m_j .
 365 This is a symmetrical equation, which satisfies Newton's third law of
 366 motion (see (Gray et al., 2001)).

- 367 • The continuity equation is discretized as :

$$\left(\frac{\partial \rho}{\partial t}\right)_i = \rho_i \sum_j \frac{m_j}{\rho_j} (\vec{v}_i - \vec{v}_j) \vec{\nabla} W_{ij} \quad (5)$$

368 This equation was chosen because it makes the density variation be
 369 zero when the fluid flow is uniform.

- 370 • Artificial linear and quadratic viscosity terms were used as suggested
 371 in (Monaghan and Gingold, 1983) to stabilize the calculations in the
 372 case of shocks.
- 373 • The equations were expressed in the current configuration according to
 374 an updated Lagrangian formulation.

375

376 The water column was discretized using about 112,000 SPH particles of
 377 radius $R_{sph} = 1.025 \text{ mm}$. Let us note that the particles were rather coarse
 378 compared to the dimensions of the specimen's opening : for example, the
 379 discretization used respectively 7 and 10 SPH particles for the circular holes
 380 of diameters $d = 14 \text{ mm}$ and $d = 20 \text{ mm}$. Indeed, SPH calculations represent

381 a high CPU cost and the available computer resources did not allow the use
382 of a larger number of particles.

383 4.3. *Fluid-structure interactions*

384 Two methods of handling the interactions between the fluid and the solid
385 parts of the model were tested :

- 386 • The pinball method, which was initially developed for solid contact
387 mechanics (Belytschko and Neal, 1991) and implemented into the EU-
388 ROPLEXUS code for both finite elements (Casadei, 1973) and SPH
389 particles (Maurel et al., 2009). In this approach, finite elements are
390 filled with spheres, called pinballs, and the contact constraints are ap-
391 plied to these spheres rather than to the elements themselves. The
392 treatment of interpenetration reduces to a simple check of the distance
393 between two spheres. If d_{12} is the distance between the centers of the
394 two pinballs and R_1, R_2 are their radii, interpenetration occurs if :

$$d_{12} < R_1 + R_2 \quad (6)$$

395 This procedure is symmetrical because both solids play the same role
396 and no distinction between a master and a slave is needed. Once contact
397 has been detected, the contact forces are calculated by enforcing the
398 impenetrability of the two impacting bodies. Lagrange multipliers ra-
399 ther than penalty functions were used, which required the introduction
400 of a user-adjustable parameter. The contact forces must be such that
401 for a nonviscous fluid :

$$(\vec{v}_1 - \vec{v}_2) \cdot \vec{n} = 0 \quad (7)$$

402 where \vec{v}_1, \vec{v}_2 are the velocities of the pinballs and \vec{n} a suitable di-
 403 rection normal to the contact surface. Much of the effectiveness and
 404 performance of the pinball algorithm depends on the choice of the ex-
 405 pressions of \vec{v}_1, \vec{v}_2 and \vec{n} . In the particular case of the interaction
 406 between an SPH fluid particle and a shell finite element, the normal \vec{n}
 407 is chosen to be the normal to the shell pinballs. This method is intended
 408 primarily for problems in which sliding and friction are not crucial : for
 409 example, in the case of two sliding planar bodies, oscillations perpen-
 410 dicular to the interface (because of the large radius of a single pinball
 411 per element) create problems. Moreover, the accuracy of the method
 412 in the case of highly distorted or irregular elements, or elements with
 413 a small topological thickness (e.g. beams or shells), is questionable.

- 414 • A master-slave method, sometimes called the sliding line method (2D)
 415 or the sliding surface method (3D) (Hallquist et al., 1985). One of the
 416 bodies in contact is designated as the master and the other as the
 417 slave. Interpenetration is detected by checking each slave node against
 418 the surface around the nearest master node. In the case of penetra-
 419 tion, suitable contact forces are applied to the bodies. These forces can
 420 be calculated using a penalty method or a Lagrange multiplier. The
 421 Lagrange multiplier approach was chosen for this work. The master-
 422 slave method has several drawbacks : the interpenetration check re-
 423 quires complex geometric calculations (and some pathological contacts
 424 can remain undetected) ; the definition of some contact surfaces by the
 425 user may require voluminous input data ; the concept of master and
 426 slave entities is artificial and creates a lack of symmetry in the formu-

427 lation which makes the results depend upon the choice made by the
428 user. However, it is often preferable to define as the master the body
429 which is likely to be penetrated by the slave.

430

431 The capabilities of the two approaches to handle the fluid-structure in-
432 teractions of the model shown in Figure 16 were tested.

433 The pinball method was found to produce poor results for the sliding
434 contact between the cylinder shells and the SPH fluid particles. Indeed, due
435 to the radii of the spheres, the normals were not exactly perpendicular to
436 what can be viewed as the common interface of the two bodies in contact.
437 The resulting contact force components tangent to the interface, even though
438 they were small, produced undesired friction-like spurious effects which im-
439 paired the free relative sliding of the two bodies. Therefore, the master-slave
440 approach was preferred for modeling the contact between the cylinder shells
441 and the SPH fluid particles. In this particular case, the choice of the mas-
442 ter and slave bodies was straightforward because SPH particles can be only
443 slaves penetrating the finite element shells.

444 Contact between the SPH fluid and the aluminium specimens was handled
445 using either sliding surfaces for specimens modeled by finite elements (no
446 crack propagation) or the pinball method for specimens modeled by SPH
447 shells (crack propagation).

448 Contact between the SPH fluid and the piston, which involves a rigid
449 body for which the master-slave method is inapplicable, was handled using
450 the pinball method.

451

452 *Remark : in the case of the SPH shell model, cylindrical pinballs were sub-*
453 *stituted for spherical pinballs in order to take into account the topological*
454 *thickness of the shell.*

455

456 **5. Comparison of the numerical and experimental results**

457 Tests E20A2 and E20A5 were studied first because they are the simplest
458 and are representative of the series of tests 1 to 10. They were chosen because
459 of the specimens' larger hole which minimized the effect of the coarse SPH
460 fluid model. Tests FUA2 and FUA5 were also simulated because, in that
461 case, the bottom was thin and the opening of the tongue at a precise angle
462 enabled us to verify the validity of the model. Then, test TF14A5 was studied
463 in order to test the capability of the model to predict fracture as a result of
464 a pressure shock. Finally, the crack propagations observed during test FXA5
465 were simulated.

466 *5.1. Tests E20A2 and E20A5*

467 These tests were simulated using two different boundary conditions for
468 the specimen, as shown in Figure 18. Indeed, one can either consider that
469 only the part of the specimen in contact with water is significant (Calculation
470 1) or try to position the built-in boundary more realistically (Calculation 2).
471 The comparison of the two calculations enabled us to assess the influence of
472 the boundary conditions on the results.

473 The pressure curves obtained with the two calculations are shown in Fi-
474 gures 19 and 20 (zoom). One can note that the pressure peak and variations

475 immediately following the impact were correctly estimated. This is a welcome
 476 conclusion because this information is important in order to predict the pos-
 477 sible rupture of the structure. However, after $t = 2 \text{ ms}$, the flow became
 478 steady and both the calculated pressure and its frequency of variation ap-
 479 peared to be too high by a factor of about 2 for Calculation 2. The error was
 480 even worse in the case of Calculation 1. A comparison of the results of the
 481 two calculations leads one to conclude that small variations in the model's
 482 boundary conditions can lead to significant variations in the pressure signal.
 483 This problem is typical of the weakly compressible model used, for which a
 484 small variation in volume can lead to a significant pressure variation through
 485 the use of a state equation of the type :

$$\delta p = c^2 \delta \rho \quad (8)$$

486 where p denotes the pressure, c the sound velocity in water and ρ the mass
 487 density. Indeed, one can observe that a small error in the estimation of the
 488 mass density (due, e.g., to geometrical inaccuracies in the model or to a
 489 weakly consistent divergence operator) leads to high pressure variations by
 490 means of the state equation 8. The example of water yields $\delta p \sim 20 \times 10^5 \delta \rho$
 491 because $c = 1450 \text{ m/s}$, *i.e.*, for $\delta \rho = 1 \text{ kg/m}^3$, $\delta p \sim 20 \text{ bars}$. This aspect
 492 has been signaled in the literature on the hydrodynamic SPH method, for
 493 example in Reference (Lee et al., 2010). Some authors attempted to improve
 494 the estimation of the pressure by using Moving Least Square (MLS) func-
 495 tions (Colagrossi and Landrini, 2003), by applying filters to various quantities
 496 (Dalrymple and Rogers, 2006) or by using an incompressible approach (Lee
 497 et al., 2006).

498 Thus, our idealized model is likely to be a little too stiff, leading to an

499 overestimation of the pressure. Moreover, the coarseness of the SPH fluid
500 model probably contributes to underestimating the leakage flow, which also
501 induces an overpressure in the model. These tendencies, as explained before,
502 are further amplified by the use of a weakly compressible model. A mesh
503 which would be both more accurate (including the visualization space, the
504 fastening screws, or even the whole drop tower) and more refined (SPH fluid
505 discretization) along with an improved fluid model would probably lead to
506 better results.

507 The other quantities obtained in the simulation matched the experimental
508 data correctly. Figure 21 shows the trajectory of the carriage. Figure 22
509 shows the outgoing velocity of the water jet, which was calculated at 97 m/s ,
510 close to the estimated 92 m/s obtained from the film recorded by the high-
511 speed camera. Finally, Figure 23(b) gives the shape of the jet at $t = 3\text{ ms}$.
512 One can observe the presence of bulbs which are comparable, although less
513 pronounced, to those observed experimentally in Figure 8(a). The simulation
514 showed that these bulbs are associated with local variations in the velocity
515 field in the jet as a direct consequence of the periodical pressure variations
516 in the cylinder.

517 The results of test E20A2 are similar and will be mentioned only briefly.
518 Here, as in all subsequent simulations, only the boundary condition corres-
519 ponding to Calculation 2 was used. The pressure curves, which are similar
520 to the previous ones, are shown in Figure 26. The water outflow velocity
521 obtained through the simulation was about 44 m/s , which is close to the
522 experimental value of about 45 m/s , as shown in Figure 27.

523 *5.2. Tests FUA2 and FUA5*

524 Let us now present and analyze the results of tests FUA2 and FUA5.
525 These calculations were similar to the previous ones because no cracking oc-
526 curred. In these two cases, the specimen was thin ($e_p = 2\text{ mm}$ and included
527 a 20 mm -wide U-shaped notch. This formed a tongue which, under the ap-
528 plied pressure, flexed and opened to a precise angle which was a function of
529 the impact velocity. The interesting aspect of this test was for us to verify
530 whether the model is capable of predicting the correct opening angle, *i.e.*
531 handling the FSIs around the notch correctly. As before, the bottom was
532 meshed using Q4GS finite elements because there was no propagating crack.
533 The notch was modeled simply by duplicating the nodes along the cutting
534 line.

535 The pressure curve obtained by the calculation for test FUA5 is shown
536 and compared to the experimental results in Figure 28; a zoom on the impact
537 zone is shown in Figure 29. The conclusions are the same as for the previous
538 tests : the pressure estimate is good immediately after the impact, then
539 deteriorates once the flow becomes steady. After $t = 2\text{ ms}$, one can see
540 that the pressure is overestimated by a factor of 2 and that the periodical
541 variations in the calculated signal have disappeared.

542 Figure 30 shows a global view of the model at $t = 3.5\text{ ms}$ while Figure 31
543 compares the experimental and numerical deflections of the specimen. There
544 is an inherent error in that the numerical deflection, which still contains
545 elastic strains (because the calculation was stopped before all the water had
546 been ejected), is compared to the experimental deflection, which contains only
547 plastic strains. Nevertheless, it is legitimate to neglect these elastic strains

548 because the total strains are very large (about 2 % for test FUA5 and 1.8 %
549 for test FUA2). The calculated opening angle α , equal to about $\alpha \sim 50^\circ$, is
550 very close to the experimental value. This shows that the FSIs around the
551 specimen were correctly taken into account, which is also confirmed by loo-
552 king at the strains near the zone where the tongue flexed, for which Figure
553 32 shows similar experimental and numerical results.

554

555 The numerical results of test FUA2 were slightly less good, but similar.
556 They will be presented only briefly. The pressure curves are given in Figures
557 33 and 34 (zoom) and present the same characteristics as before. The opening
558 angles of the tongue are compared in Figure 35. One can note that the match
559 is less good than for test FUA5 because the opening predicted by the model
560 seems a little too wide. The explanation probably lies in the coarse mesh used
561 for the SPH fluid : indeed, a rapid calculation shows that for $\alpha \sim 20^\circ$ the
562 size of the opening is about 3 SPH particles, which is very coarse. Therefore,
563 one could expect better results by using a more refined SPH discretization.

564 5.3. Test TF14A5

565 Like tests F14A2-5 and TFA5, test TF14A5 presented a ruptured bottom
566 along the spot-facing circumference. The final state of the specimens is given
567 in Figure 14. This phenomenon, which had not been anticipated at the time
568 the specimens were designed, is due to the presence of stress concentrations,
569 particularly shear stresses, at the level of the junction between the thin part
570 and the thick bottom.

571 *5.3.1. The damage model*

572 The crack's path was known and simple, which enabled the fractured
 573 specimen to be modeled using the FEM. In order to do that, we meshed the
 574 bottom using Q4GS finite elements again, and Von Mises' plasticity theory
 575 was coupled with Lemaitre and Chaboche's damage theory (Lemaitre et al.,
 576 1985).

577 In this case, the damage originates in the shear strain, which induces
 578 plasticity, and in the volume strain, which induces the growth of cavities and
 579 cracks. By expressing that the damage is governed by the shear and volume
 580 strain energies (Lemaitre et al., 1985), one obtains the following damage
 581 criterion f_D :

$$f_D = \left[\frac{2}{3}(1 + \nu) + 3(1 - 2\nu) \left(\frac{\sigma_H}{\sigma_{eq}} \right)^2 \right] p - \epsilon_p^s \leq 0 \quad (9)$$

582 where σ_H denotes the hydrostatic stress, σ_{eq} Von Mises' equivalent stress,
 583 σ_H/σ_{eq} the triaxiality rate of the stresses and ϵ_p^s the threshold equivalent
 584 plastic strain. This criterion is known as the elastic energy density recovery
 585 rate criterion. The evolution of the damage is given by Lemaitre and Chabo-
 586 che's law (Lemaitre et al., 1985) :

$$\dot{D} = \frac{D_c}{\epsilon_p^c - \epsilon_p^s} \left[\frac{2}{3}(1 + \nu) + 3(1 - 2\nu) \left(\frac{\sigma_H}{\sigma_{eq}} \right)^2 \right] \dot{p} \quad (10)$$

587 Three material parameters play a role in the evolution of the damage :

- 588 • the threshold equivalent plastic strain ϵ_p^s beyond which damage occurs,
 589 *i.e.* cavities and microcracks begin to grow,
- 590 • the critical equivalent plastic strain ϵ_p^c beyond which fracture of the
 591 material occurs,

592 • the critical damage D_c reached when $\epsilon_p = \epsilon_p^c$. Physically, D_c represents
593 the volume fraction of the defects at the fracture point.

594 Classically, this damage model is affected by a mesh dependency problem.
595 Indeed, simulations involving a material with a negative stress-strain slope
596 fail to give satisfactory results in the sense that, close to fracture, strains
597 and damage are often artificially localized within a single mesh element.
598 Thus, the path of what one may call the crack depends on the position of
599 the elements. Moreover, if one refines the mesh, the damaged zone remains
600 limited to the width of an element and critical damage is reached more rapidly
601 (D_c is reached after a constant number of time steps). Thus, the energy
602 dissipated in the fracture and the time to fracture tend to zero for an infinitely
603 refined mesh. This is not physically consistent because it would require an
604 infinite growth rate of the microcracks and cavities.

605 It was proven in (Bazoant and Belytschko, 1985; Needleman, 1988) that
606 the origin of the problem resides in the transformation of the initial hyper-
607 bolic problem into an ill-posed elliptic problem when the material softens.
608 Then, the propagation velocity of the waves becomes complex. Thus, the
609 first element of the mesh which assumes softening behavior fails to transmit
610 strains to its neighbors, which creates the problems mentioned previously.

611 The solutions proposed by the community to alleviate this difficulty consist
612 in preserving the hyperbolic character of the equations. Most of these solu-
613 tions boil down to treating the damage in a nonlocal manner by introducing
614 a characteristic length or a characteristic time which reflects the interaction
615 of one entity of the mesh with the others. In this work, we chose to introduce
616 a characteristic time by using a model with a delay effect (Ladeveze, 1991;

617 Ladevèze, 1992).

618 Consequently, the previous damage law was modified as follows :

$$\dot{D}_{nc} = \frac{D_c}{\epsilon_p^c - \epsilon_p^s} \left[\frac{2}{3}(1 + \nu) + 3(1 - 2\nu) \left(\frac{\sigma_H}{\sigma_{eq}} \right)^2 \right] \dot{p} \quad (11)$$

619 \dot{D}_{nc} being what we call the uncorrected damage. Then the damage rate is
620 given by (Allix and Deu, 1997) :

$$\dot{D} = \frac{1}{\tau_c} (1 - \exp(-a \langle D_{nc} - D \rangle)) \quad (12)$$

621 where τ_c and a are two material coefficients ; “ $\langle . \rangle$ ” denotes the positive part
622 operator ; τ_c represents the inverse of the maximum damage rate. An accurate
623 identification of the parameters of the constitutive law, especially concerning
624 damage, plays a key role in obtaining good results. These parameters were
625 identified in (Suffis, 2004) and are given in Table 6.

626

627 In order to avoid mesh dependency, the mesh should verify $\Delta l < l_{car}$,
628 where l_{car} and Δl denote respectively the characteristic length of the fully
629 damaged zone and the element size. It was shown in (Suffis et al., 2003) that
630 l_{car} can be approximated by :

$$l_{car} \simeq c \tau_c \ln\left(\frac{\Delta\sigma}{\sigma_{lim}}\right) \quad (13)$$

631 where $\Delta\sigma$ is the stress jump caused by the impact and σ_{lim} is such that :

$$E\epsilon_p^s < \sigma_{lim} < E \left(\epsilon_p^s + 3 \frac{E\epsilon_p^c - E\epsilon_p^s}{a} \right) \quad (14)$$

632 E being the material’s Young’s modulus.

633 $\Delta\sigma$ can be approximated through a simple analytical calculation of an
634 idealized circular plate with no hole. As a consequence, the element size in

635 the damaged zone is such that $\Delta l < 1.5mm$. In order to have several elements
636 in the damage zone, we chose $\Delta l = 0.5mm$.

637 Once an element has become fully damaged, it is eroded, *i.e.* removed
638 from the model. In order to prevent any loss of mass (and, therefore, of
639 energy) during the calculations, the eroded elements are replaced by debris
640 represented by spheres of equivalent mass. These spheres are shown in red in
641 Figure 36.

642 5.3.2. Comparison with experimental results

643 Figure 36 presents the numerical model of test TF14A5 at $t = 2.5 ms$.
644 The time to fracture was determined experimentally at $t \sim 1.5 ms$ using the
645 pressure curve, in which it corresponds to a sharp drop in the signal (see
646 Figure 37). The pressure curve obtained with the model, shown in Figure 37,
647 agrees well with the experimental results in terms of amplitudes, variations
648 and time to fracture, which was also calculated at about $t \sim 1.5 ms$. Curve 38
649 confirms the good quality of the simulation because one can observe matching
650 experimental and numerical deflections of the specimen at a distance $(D_{ext} +$
651 $d)/4$ from the center of the hole.

652 These results confirm that the numerical model is capable of predicting
653 post-impact phenomena accurately, including the possible rupture of the spe-
654 cimen.

655 5.4. Test FXA5

656 Finally, let us study test FXA5. The specimen used was thin ($e_p = 2 mm$)
657 and included two 30 mm precracks forming a cross. As a result of the pres-
658 sure shock, the cracks propagated; then the petals thus formed opened up

659 and let the fluid escape. The state of the specimen at the end of the test is
 660 shown in Figure 39, with the cracks' paths marked in red. This test is espe-
 661 cially interesting because it enables us to test the capability of the model to
 662 reproduce the cracking process and the resulting opening of the petals.

663 5.4.1. The SPH shell model

664 The FE model used previously cannot account for crack propagation and
 665 could not be used to simulate test FXA5. In this case, we studied the spe-
 666 cimen using a shell model based on the SPH meshless method. This SPH
 667 shell model (SPHS) was developed in (Maurel and Combescure, 2008) and is
 668 especially suitable for modeling cracks, as proven in (Caleyron et al., 2011).
 669 The reader can refer to these works for a detailed description of the model.
 670 Only the main points will be reviewed here.

671 *Formulation.* The SPHS formulation is based on the Mindlin-Reissner theory
 672 and relies on the assumption that the thickness e of the structure is small
 673 compared to its other dimensions. Thus, one can write :

$$\vec{x}(t) = \vec{x}_m(t) + \xi \vec{n}(t) \quad \xi \in \left[-\frac{e}{2}; +\frac{e}{2}\right] \quad (15)$$

674 where \vec{x}_m denotes the position of the point in the mean plane of the shell and
 675 \vec{n} is the pseudo-normal which materializes the orientation of the material.
 676 The theory takes into account transverse shear, so \vec{n} is not necessarily normal
 677 to the mean plane.

678 The original SPH method (Gingold and Monaghan, 1977) suffers from
 679 a numerical instability known as tension instability. Indeed, the authors of
 680 (Wen et al., 1994) showed that the Eulerian kernel used classically is uns-
 681 table in the presence of tension stresses. The solution chosen for the SPHS

682 model was taken from (Belytschko et al., 2000) and consists in using a total
683 Lagrangian formulation whose kernel is stable.

684 Therefore, the SPH shell is studied using the total Lagrangian formalism,
685 in which the membrane, transverse shear and bending strains are calculated.
686 Then, the application of a plane stress constitutive relation leads to the
687 corresponding stresses. These stresses are integrated across the thickness in
688 order to obtain the stress resultants of the shell. Finally, the equilibrium of
689 the shell is expressed as a function of the generalized membrane loads $\underline{\underline{N}}$ and
690 transverse shear loads \overrightarrow{T} and of the bending moments $\underline{\underline{M}}$.

691 *Discretization.* The global response of the structure is described in its mean
692 plane, which is discretized using a single layer of SPH nodes. Each node can
693 be viewed as a cylinder with its axis normal to the shell, its thickness e and
694 its radius chosen as a function of the desired mesh fineness. The nodes have
695 5 degrees of freedom because the “drilling rotation” is not taken into account
696 (see Figure 40).

697 The spatial discretization requires the introduction of shape functions
698 allowing the representation and the derivation of a data field. In order to
699 do that, we use MLS functions as described in (Dilts, 1999, 2000). These
700 functions are built from an n^{th} -order polynomial basis, which gives them n^{th} -
701 order consistency. Second-order functions are used for the approximation of
702 the field of the pseudo-normals \overrightarrow{n} in order to achieve a good representation
703 of the curvature of the shell. First-order functions are used for the derivation
704 operations. The reader can refer to (Dilts, 1999; Belytschko et al., 1994b) for
705 details concerning the construction of these functions.

706 Finally, the use of collocation for strong formulations such as the SPH

707 method leads to the occurrence of zero-energy modes. (Belytschko et al.,
708 2000) presented a complete study of this problem and showed that the use of
709 a total Lagrangian formulation reduces these instabilities. However, this is not
710 sufficient in the case of the SPH model because the field of the normals to the
711 mean surface is sensitive to the presence of instabilities affecting the curvature
712 of the shell. Since the problem comes from the fact that the kinematic fields
713 and the strain and stress fields are supported by the same nodes, (Belytschko
714 et al., 2000; Dyka et al., 1997) proposed the introduction of a second type
715 of nodes called Stress Points (SP). No material is attached to these points,
716 which play a role similar to that of Gauss points in the FEM : the strain and
717 stress fields are calculated at the SPs using the kinematic quantities at the
718 nodes, then the equilibrium equations are written back at the nodes again.
719 The number and the positions of the SPs are parameters of the method.

720 Consequently, the constitutive relation of the material is applied at the
721 model's SPs. The law used for test FXA5 was identical to that presented in
722 Section 5.3.1. The difference resided in the use of a global model based on
723 Ilyushin's theory (Ilyushin, 1956) because only one SP was used through the
724 thickness of the shell.

725 *Fracture.* The SPHS model was extended to the modeling of fracture in (Ca-
726 leyron et al., 2011). When the damage calculated at a particular SP reaches
727 its critical value D_c , the Elementary Representative Volume (ERV) suppor-
728 ted by the SP is considered to be fractured. Fully damaged ERVs are treated
729 as strong discontinuities, which is an efficient way to address cases where the
730 crack's lips separate significantly. The method we implemented consists of
731 four stages :

- 732 • application of the free edge condition to the neighboring nodes of the
733 cracked ERV ;
- 734 • elimination of the links cutting the cracked ERV by means of the visi-
735 bility method (Belytschko et al., 1994a),
- 736 • treatment of the fragments, *i.e.* the nodes which no longer have neigh-
737 bors ;
- 738 • updating of the MLS functions.

739 Thus, in this model, a crack is represented by a series of cracked ERVs, as
740 shown in Figure 41. These ERVs are supported by the SPs of the model. This
741 method is attractive because it does not require an explicit representation of
742 the cracks, which enables one to deal with multicracking and crack branching
743 easily.

744 *5.4.2. Comparison with experimental data*

745 The SPHS model presented previously was introduced locally over the
746 specimen’s mesh through a coupling with the Q4GS elements, as shown in
747 Figure 42. This coupling was of the Arlequin type : the equality of velocities
748 was enforced weakly over a common zone called the overlapping zone, in
749 which the energies of the two models are blended. The theory is not described
750 in this paper. The reader can refer to (Ben Dhia and Rateau, 2004; Bauman
751 et al., 2008; Chuzel-Marmot et al., 2011; Caleyron, 2011) for further details.

752 The FE and SPHS models used the same constitutive law, which was
753 that used for test TF14A5 (see Section 5.3), *i.e.* a Von Mises’ plasticity law
754 coupled with Lemaitre and Chaboche’s damage : the model was global for
755 the SPHS and integrated through the thickness with 5 Gauss points for the
756 finite elements. The contact between the SPH shell and the SPH fluid model

757 was handled through the pinball method. The other contacts were handled
758 through the sliding surface method. The SPHS discretization required about
759 15,000 nodes and SPs with a radius $R_{sph} = 0.35 \text{ mm}$.

760 Figure 43 shows the state of the model at $t = 2.1 \text{ ms}$. The behavior was
761 satisfactory because one can indeed observe a propagation of the cracks and
762 the associated opening of the petals.

763 The experimental and numerical crack paths and sizes are compared in
764 Figure 44. The crack lengths appear to be slightly overestimated, due prob-
765 ably to the coarse fluid discretization exaggerating the opening of the shell.
766 Nevertheless, the simulated paths are consistent with those observed experi-
767 mentally since, in both cases, the cracks propagated in mixed mode. These
768 curved paths led to the opening of two of the four petals, marked with a
769 “+” sign on the figure. One should also note the branching of the two cracks,
770 which was not observed experimentally. This branching seems to occur near
771 the overlapping zone of the Arlequin coupling, which suggests that the SPHS
772 domain used was a little too small, leading to nonlinear phenomena in the
773 overlapping zone which may have been responsible for errors in the crack’s
774 propagation.

775 Even though a more refined fluid discretization could have led to better
776 results, the comparison of the numerical and experimental results is satis-
777 factory. The model we implemented enables one to predict effectively the
778 fracture of a tank subjected to impact and the associated leakage flow.

779 **6. Conclusions**

780 This paper presented and studied an experiment which is representative of
781 an impact on a fluid-filled tank. The results of this experiment were compared
782 with those of a numerical model.

783 First, the study of tests which presented no fracture or crack propagation
784 gave us an understanding of the phenomena involved in the experiment. In
785 particular, we showed that the impacted tank behaves as a true oscillator
786 in which the fluid and structural phenomena are coupled in a nonperma-
787 nent way. Consequently, the prediction of the behavior of an impacted tank
788 requires a precise modeling of the fluid, the thin structure and their inter-
789 actions. The numerical model we proposed studies the fluid using the SPH
790 meshless method. This method is especially suitable for impacts involving
791 fluids with significant free surface variations. In addition, the main structu-
792 ral elements (the cylinder, the piston and the specimen) were modeled in
793 order to represent the stiffness of the experimental setup accurately. Finally,
794 the nonpermanent fluid-structure interactions were handled by means of the
795 sliding surface method. The numerical results obtained were satisfactory,
796 particularly concerning the prediction of the quantities of interest immedi-
797 ately following the impact. The fluid outflow velocity, the displacement of
798 the carriage and the deflection of the specimen were correctly predicted by
799 the model. The pressure peak which immediately followed the impact was
800 correctly estimated, too, which is an important point with regard to the pre-
801 diction of the failure of the tank. However, once the flow had become steady,
802 the pressure in the cylinder was incorrectly predicted since the calculated
803 values were up to twice those measured experimentally. These inaccuracies

804 are due to the fluid model, which is suitable for impact analysis, but less
805 effective in the case of stationary flows. Then, more complex tests involving
806 the propagation of cracks and, in some cases, the complete rupture of the
807 specimen were studied. We started out by showing that the model is capable
808 of predicting the complete failure of the tank accurately. In order to do that,
809 we used a damageable elastic-plastic constitutive relation with a delay effect.
810 An accurate identification of the parameters, especially the delay effect, was
811 found to be a key factor in obtaining good results. Finally, we studied a test
812 presenting a more complex crack path. In this case, the FE model was re-
813 placed by a meshless SPH shell model dedicated to the modeling of cracks.
814 This model was introduced locally in the zone where fracture was expected,
815 which enabled us to achieve reasonable computation times.

816 In conclusion, an impacted tank behaves like a true fluid-structure oscil-
817 lator. Therefore, it is necessary to model both the structural and fluid pheno-
818 mena accurately, including the most complex of these phenomena which are
819 damage, fracture and significant free surface variations. In this context, the
820 use of meshless methods appears to be particularly attractive. Finally, the
821 fluid-structure coupling method must be capable of handling nonpermanent
822 interactions.

823 **Acknowledgements**

824 The authors wish to thank the French Atomic Energy Commission (CEA)
825 and the French Electricity Company (EDF) for their support regarding the
826 EUROPLEXUS software; ONERA for its experimental support; and the
827 EEC for its financial support concerning the test rig. F. Caleyron extends

828 his personal thanks to Jacky Fabis of ONERA Lille for helpful discussions.

829 **Références**

830 Allix, O., Deu, J., 1997. Delayed-damage modelling for fracture prediction
831 of laminated composites under dynamic loading. *Engineering Transac-*
832 *tions/Rozprawy Inzynierskie* 45, 29–46.

833 Anderson, C., et al., 1999. Simulation and analysis of a 23-mm hei projectile
834 hydrodynamic ram experiment. *International journal of impact engineering*
835 22, 981–997.

836 Bauman, P., Ben Dhia, H., Elkhodja, N., Oden, J., S., P., 2008. On the ap-
837 plication of the arlequin method to the coupling of particle and continuum
838 models. *Computational Mechanics* 42, 511–530.

839 Bazoant, Z., Belytschko, T., 1985. Wave propagation in a strain-softening
840 bar : exact solution. *Journal of engineering mechanics* 111, 381–389.

841 Belytschko, T., Gu, L., Lu, Y., 1994a. Fracture and crack growth by element
842 free galerkin methods. *Modelling and Simulation in Materials Science and*
843 *Engineering* 2, 519.

844 Belytschko, T., Guo, Y., Liu, W., Xiao, S., 2000. A unified stability analysis
845 of meshless particle methods. *International Journal for Numerical Methods*
846 *in Engineering* 48, 1359–1400.

847 Belytschko, T., Lu, Y., Gu, L., 1994b. Element-free galerkin methods. *In-*
848 *ternational journal for numerical methods in engineering* 37, 229–256.

- 849 Belytschko, T., Neal, M., 1991. Contact-impact by the pinball algorithm
850 with penalty and lagrangian methods. *International Journal for Numerical*
851 *Methods in Engineering* 31, 547–572.
- 852 Ben Dhia, H., Rateau, G., 2004. The arlequin method as a flexible engineering
853 design tool. *International Journal For Numerical Methods in Engineering*
854 62, 1442–1462.
- 855 Caleyron, F., 2011. Simulation numérique par la méthode SPH de fuites de
856 fluide consécutives à la déchirure d’un réservoir sous impact. Ph.D. thesis.
857 Université de Lyon.
- 858 Caleyron, F., Combescure, A., Faucher, V., Potapov, S., 2011. Dynamic
859 damage-fracture transition simulation for sph shells. *International Journal*
860 *for Numerical Methods in Engineering* in press.
- 861 Casadei, F., 1973. A General Impact-Contact Algorithm based on hierarchic
862 pinballs for the EUROPLEXUS software system. Technical Report.
- 863 Chao, T., Shepherd, J., 2005. Fracture response of externally flawed alumi-
864 num cylindrical shells under internal gaseous detonation loading. *Internat-*
865 *ional journal of fracture* 134, 59–90.
- 866 Chuzel-Marmot, Y., Ortiz, R., Combescure, A., 2011. Three dimensional sph-
867 fem gluing for simulation of fast impacts on concrete slabs. *Computers &*
868 *Structures* .
- 869 Colagrossi, A., Landrini, M., 2003. Numerical simulation of interfacial flows
870 by smoothed particle hydrodynamics. *Journal of Computational Physics*
871 191, 448–475.

- 872 Dalrymple, R., Rogers, B., 2006. Numerical modelling of water waves with
873 the sph method. *Coastal Engineering* 53, 141–147.
- 874 Dilts, G., 1999. Moving-least-squares-particle hydrodynamics i. consistency
875 and stability. *International Journal for Numerical Methods in Engineering*
876 44, 1115–1155.
- 877 Dilts, G., 2000. Moving least-squares particle hydrodynamics ii : conser-
878 vation and boundaries. *International Journal for Numerical Methods in*
879 *Engineering* 48, 1503–1524.
- 880 Disimile, P., Swanson, L., Toy, N., 2009. The hydrodynamic ram pressure
881 generated by spherical projectiles. *International Journal of Impact Engi-*
882 *neering* 36, 821–829.
- 883 Dyka, C., Randles, P., Ingel, R., 1997. Stress points for tension instability
884 in sph. *International journal for numerical methods in engineering* 40,
885 2325–2341.
- 886 Freitas, C., Anderson Jr, C., Goodlin, D., 1997. Hydrodynamic Ram : A
887 Review of Experimental Data for Use in Validation of Numerical Simula-
888 tions. Technical Report. SwRI Report 06-7365/001, Southwest Research
889 Institute, San Antonio, TX 78228, prepared for Wright Laboratory, Wright-
890 Patterson AFB, OH.
- 891 Freitas, C., Anderson Jr, C., Walker, J., Littlefield, D., 1996. Hydrodynamic
892 ram : a benchmark suite, structures under extreme loading conditions, pvp,
893 vol. 325. New York : ASME , 63–74.

- 894 Gingold, R., Monaghan, J., 1977. Smoothed particle hydrodynamics-theory
895 and application to non-spherical stars. *Monthly Notices of the Royal As-*
896 *tronomical Society* 181, 375–389.
- 897 Gray, J., Monaghan, J., Swift, R., 2001. Sph elastic dynamics. *Computer*
898 *methods in applied mechanics and engineering* 190, 6641–6662.
- 899 Hallquist, J., Goudreau, G., Benson, D., 1985. Sliding interfaces with contact-
900 impact in large-scale lagrangian computations. *Computer Methods in Ap-*
901 *plied Mechanics and Engineering* 51, 107–137.
- 902 Ilyushin, A., 1956. *Plasticité*. Eyrolles.
- 903 Keesecker, A., Dávila, C., Johnson, E., Starnes, J., et al., 2003. Crack path
904 bifurcation at a tear strap in a pressurized shell. *Computers & structures*
905 81, 1633–1642.
- 906 Ladeveze, P., 1991. About a damage mechanics approach. *Mechanics and*
907 *Mechanisms of Damage in Composites and Multi-materials* 35, 119–141.
- 908 Ladevèze, P., 1992. A damage computational method for composite struc-
909 tures. *Computers & structures* 44, 79–87.
- 910 Lee, E.S., Moulinec, C., Xu, R., Violeau, D., Laurence, D., Stansby, P., 2006.
911 Comparisons of weakly compressible and truly incompressible sph algo-
912 rithms for 2d flows. *Journal of Computational Physics* 227, 8417–8436.
- 913 Lee, E.S., Violeau, D., Issa, R., Ploix, S., 2010. Application of weakly com-
914 pressible and truly incompressible sph to 3-d water collapse in waterworks.
915 *Journal of Hydraulic Research* 48, 50–60.

- 916 Lemaitre, J., Chaboche, J., Germain, P., 1985. *Mécanique des matériaux*
917 *solides*. Dunod.
- 918 Maurel, B., Combescure, A., 2008. An sph shell formulation for plasticity and
919 fracture analysis in explicit dynamics. *International Journal for Numerical*
920 *Methods in Engineering* 76, 949–971.
- 921 Maurel, B., Potapov, S., Fabis, J., Combescure, A., 2009. Full sph fluid-
922 shell interaction for leakage simulation in explicit dynamics. *International*
923 *Journal for Numerical Methods in Engineering* 80, 210–234.
- 924 Monaghan, J., Gingold, R., 1983. Shock simulation by the particle method
925 sph. *Journal of Computational Physics* 52, 374–389.
- 926 Needleman, A., 1988. Material rate dependence and mesh sensitivity in lo-
927 calization problems. *Computer Methods in Applied Mechanics and Engi-*
928 *neering* 67, 69–85.
- 929 Potapov, S., Maurel, B., Combescure, A., Fabis, J., 2009. Modeling
930 accidental-type fluid-structure interaction problems with the sph method.
931 *Computers & Structures* 87, 721–734.
- 932 Rabczuk, T., Areias, P., Belytschko, T., 2007. A meshfree thin shell me-
933 thod for non-linear dynamic fracture. *International Journal for Numerical*
934 *Methods in Engineering* 72, 524–548.
- 935 Rabczuk, T., Gracie, R., Song, J., Belytschko, T., 2009. Immersed particle
936 method for fluid-structure interaction. *International Journal for Numerical*
937 *Methods in Engineering* 81, 48–71.

- 938 Sauer, M., 2010. Simulation of high velocity impact in fluid-filled containers
939 using finite elements with adaptive coupling to smoothed particle hydro-
940 dynamics. *International Journal of Impact Engineering* .
- 941 Suffis, A., 2004. Développement d'un modèle d'endommagement à taux de
942 croissance contrôlé pour la simulation robuste de ruptures sous impacts.
943 Ph.D. thesis. Université de Lyon.
- 944 Suffis, A., Lubrecht, T., Combescure, A., 2003. Damage model with delay
945 effect : : Analytical and numerical studies of the evolution of the charac-
946 teristic damage length. *International journal of solids and structures* 40,
947 3463–3476.
- 948 Timm, T., 2003. Beschuss von flüssigkeitsgefüllten Behältern. Ph.D. thesis.
949 Karlsruhe University, Germany.
- 950 Varas, D., López-Puente, J., Zaera, R., 2009a. Experimental analysis of fluid-
951 filled aluminium tubes subjected to high-velocity impact. *International*
952 *Journal of Impact Engineering* 36, 81–91.
- 953 Varas, D., Zaera, R., López-Puente, J., 2009b. Numerical modelling of the
954 hydrodynamic ram phenomenon. *International Journal of Impact Engi-*
955 *neering* 36, 363–374.
- 956 Wen, Y., Hicks, D., Swegle, J., 1994. Stabilizing SPH with conservative
957 smoothing. Technical Report. Sandia National Labs., Albuquerque, NM
958 (United States).

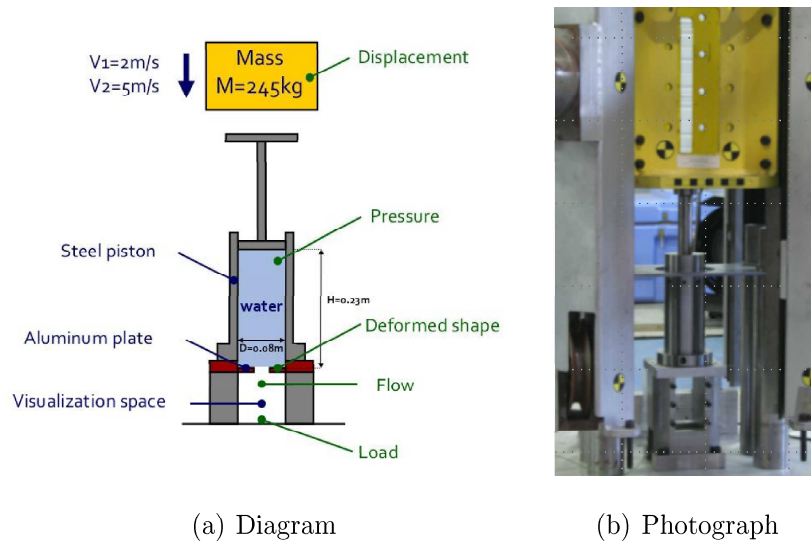


FIGURE 1: The experimental setup

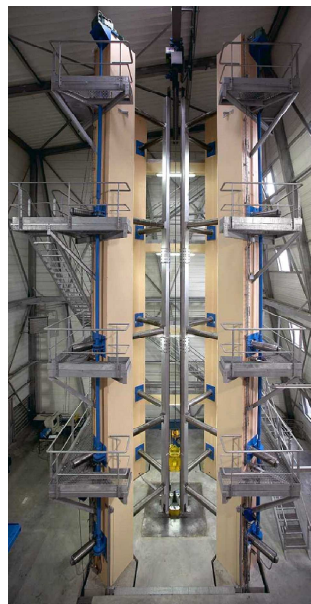


FIGURE 2: The drop tower of ONERA Lille

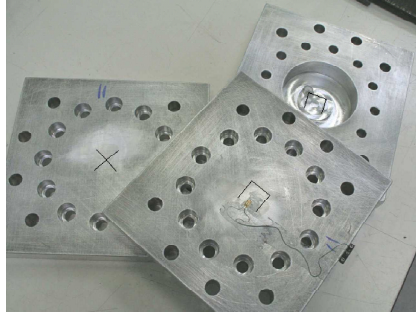
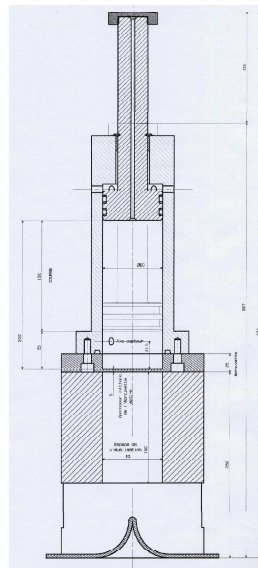


FIGURE 3: Examples of specimens before impact : X-shaped and U-shaped precracks



(a) Photograph



(b) General diagram

FIGURE 4: Overview of the experimental device

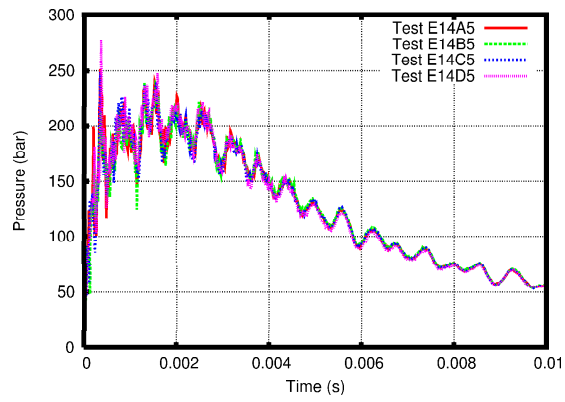


FIGURE 5: The pressure in the cylinder (tests E14A-B-C-D5)

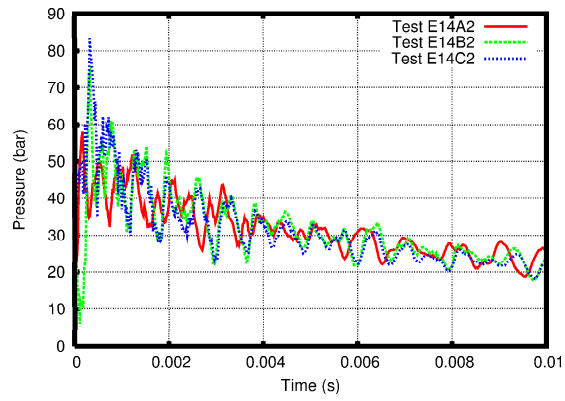


FIGURE 6: The pressure in the cylinder (tests E14A-B-C2)

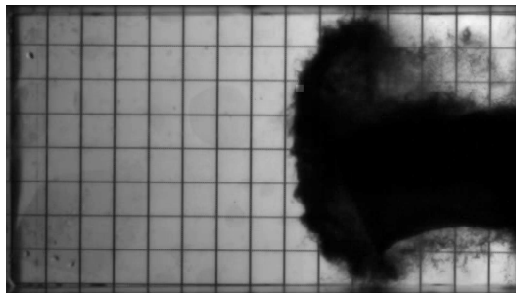


FIGURE 7: The outflow at $t = 2.5 \text{ ms}$ (test E20A2)

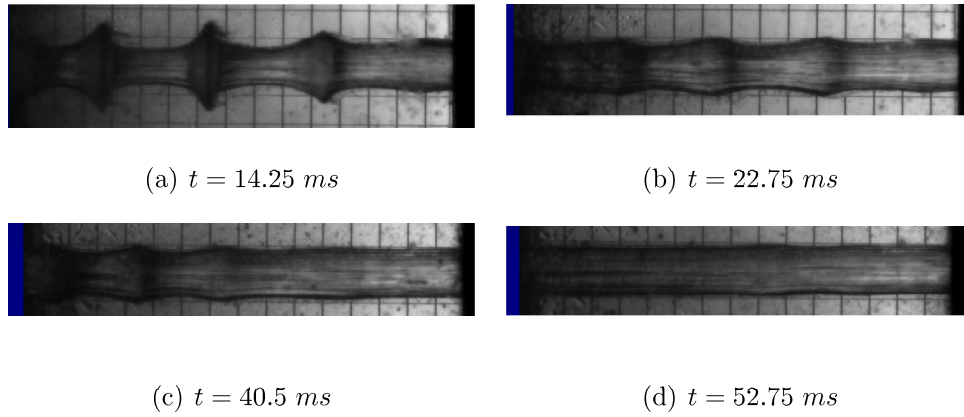


FIGURE 8: Profile of the outflow (test E20A2)

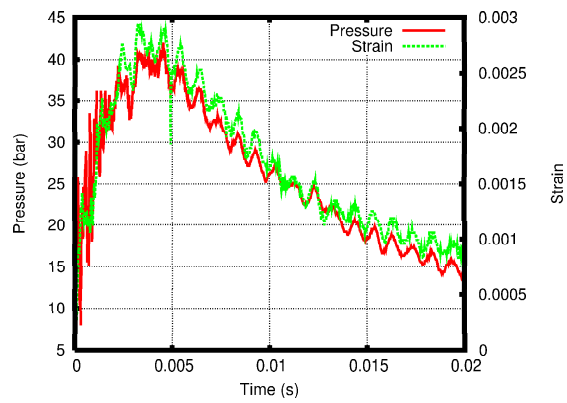
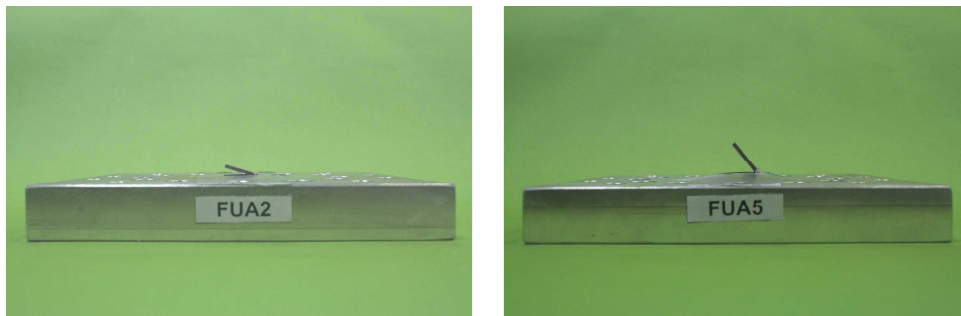


FIGURE 9: The pressure in the cylinder and deflection of the specimen (test F14A2)



(a) test FUA2

(b) test FUA5

FIGURE 10: Opening of the precrack (tests FUA2 and FUA5)



FIGURE 11: The outflow at $t = 1.75 \text{ ms}$ (test FUA5)

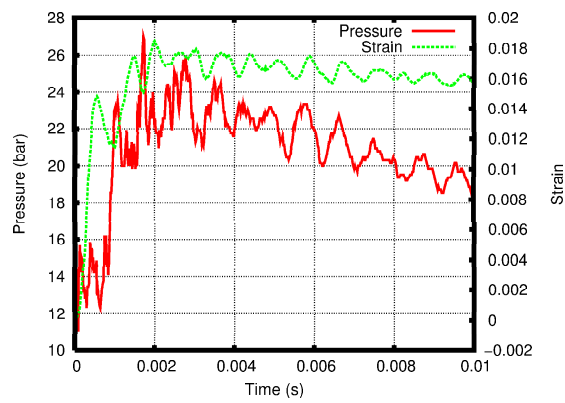


FIGURE 12: The pressure in the cylinder and deflection of the specimen (test FUA2)

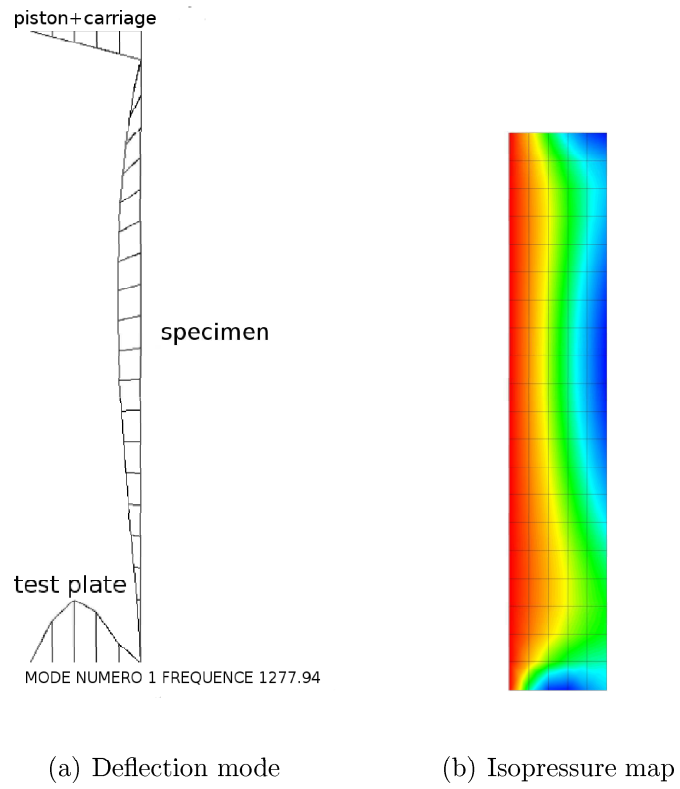
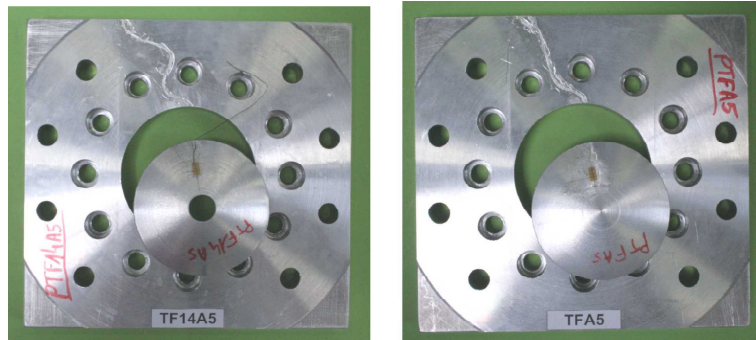


FIGURE 13: Calculation of the first mode of the water-filled piston (CASTEM)



(a) test TF14A5

(b) test TFA5

FIGURE 14: Complete rupture of the bottom (tests TF14A5 and TFA5)



(a) tests FXA2 and FXA5



(b) tests FE20A5 and F14E3A5

FIGURE 15: Propagation of the precracks

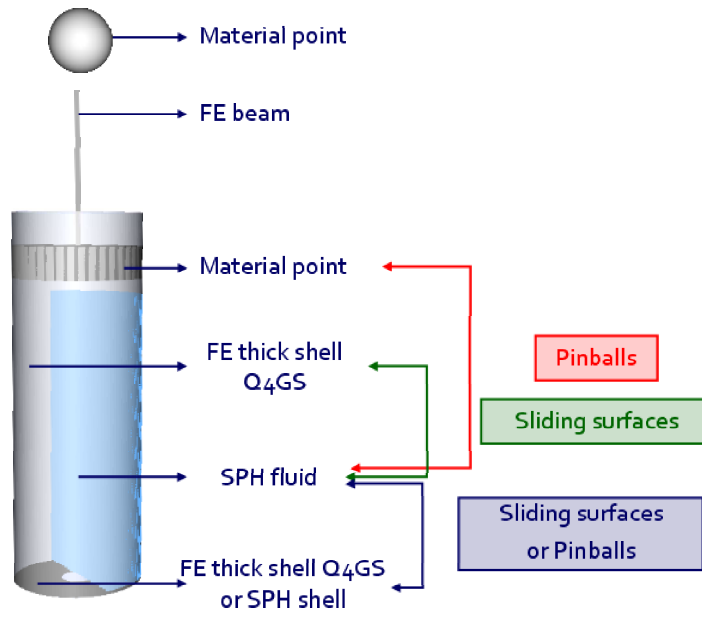
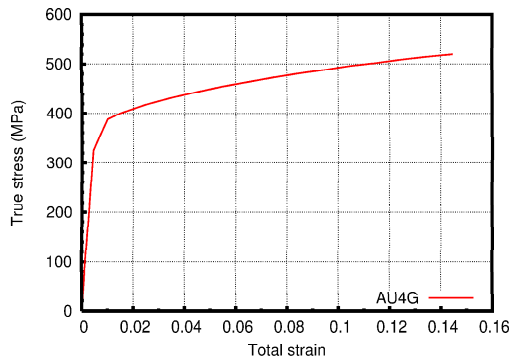


FIGURE 16: The numerical model of the experimental device



Parameter	Value
E (GPa)	73.1
ρ (kg/m^3)	2,780
ν	0.33
σ_y (MPa)	325

TABLE 1: The material parameters of

FIGURE 17: AU4G traction curve AU4G

Parameter	Value
E (GPa)	211
ρ (kg/m^3)	7,700
ν	0.3
σ_y (MPa)	900

Parameter	Value
ρ (kg/m^3)	1000
c (m/s)	1450

TABLE 3: The material parameters of

TABLE 2: The material parameters of water
APX

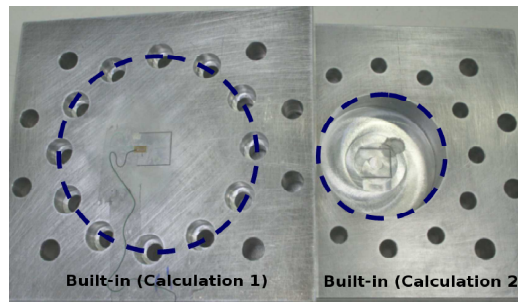


FIGURE 18: Modeling of the specimen's support

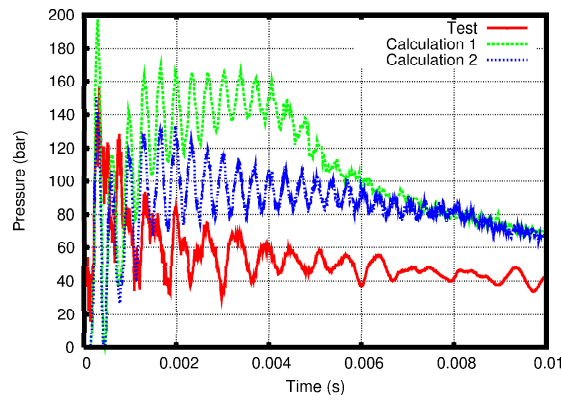


FIGURE 19: The pressure in the cylinder (test E20A5)

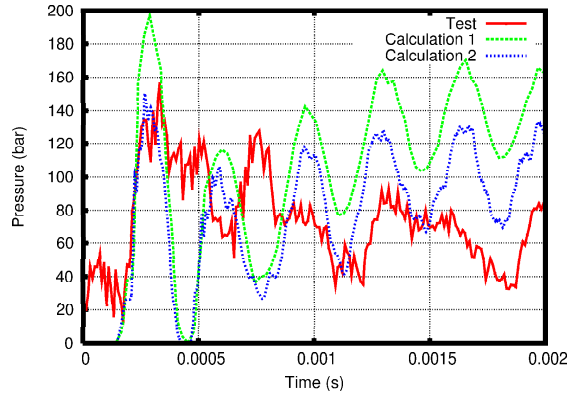


FIGURE 20: The pressure in the cylinder : zoom (test E20A5)

Remark : the pressure sensor is modeled using a simple FE node. The pressure is obtained by dividing the load applied by the fluid at the node by the area of an element.

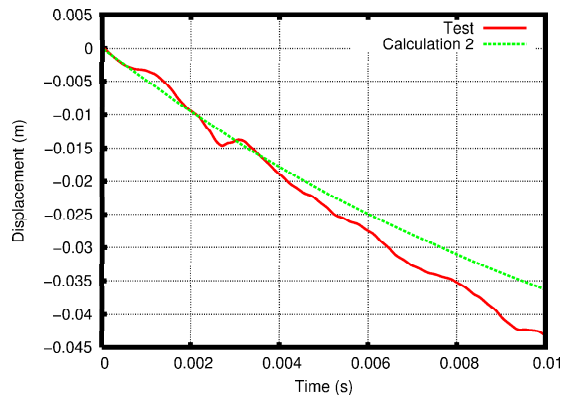


FIGURE 21: The displacement of the carriage (test E20A5)

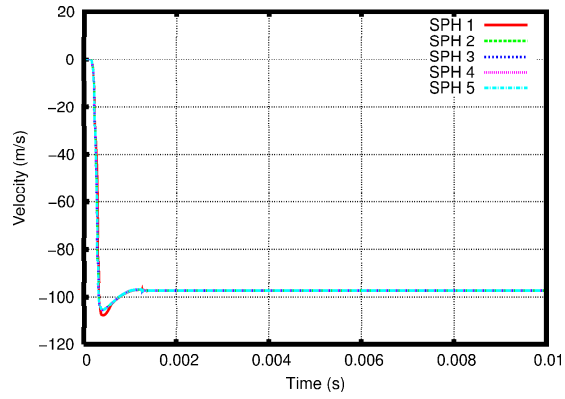
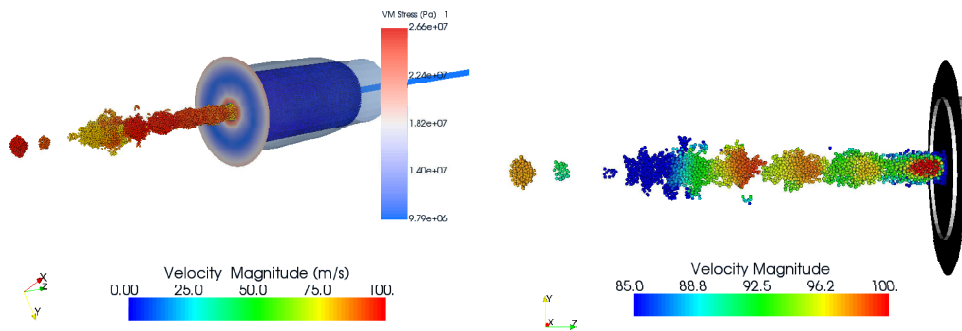


FIGURE 22: Outgoing velocity of the jet (test E20A5, Calculation 2)



(a) Velocity, Von Mises' stress and deflection of the cylinder ($\times 1,000$)

(b) Bulbs in the fluid flow

FIGURE 23: The simulation of test E20A5 at $t = 3 \text{ ms}$ (Calculation 2)

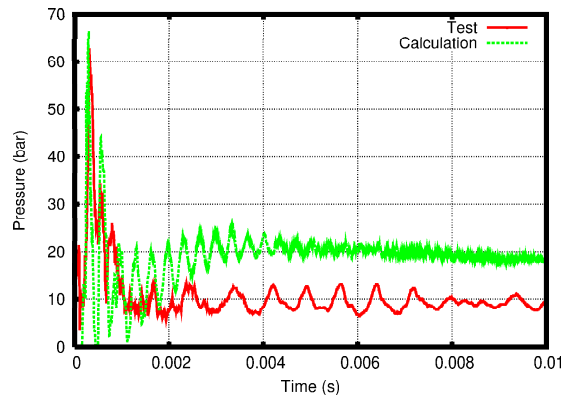


FIGURE 24: The pressure in the cylinder (test E20A2)

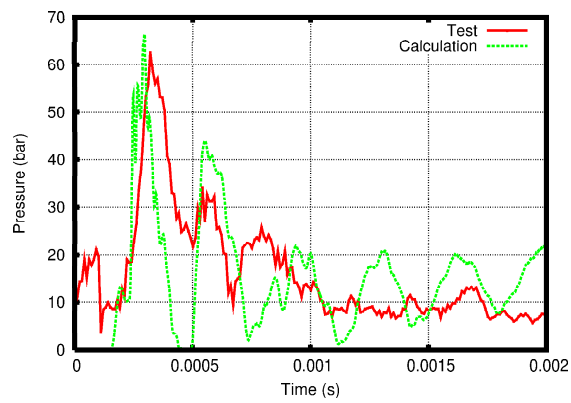


FIGURE 25: The pressure in the cylinder : zoom (test E20A2)

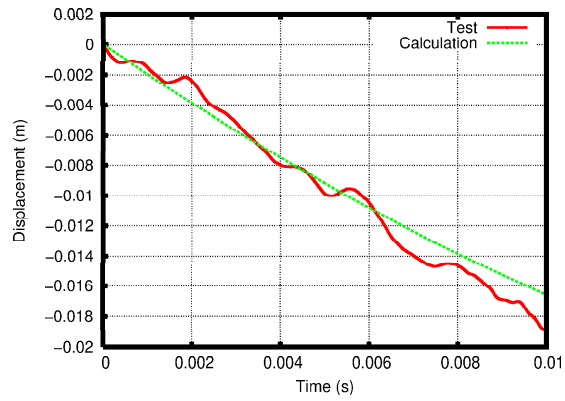


FIGURE 26: The displacement of the carriage (test E20A2)

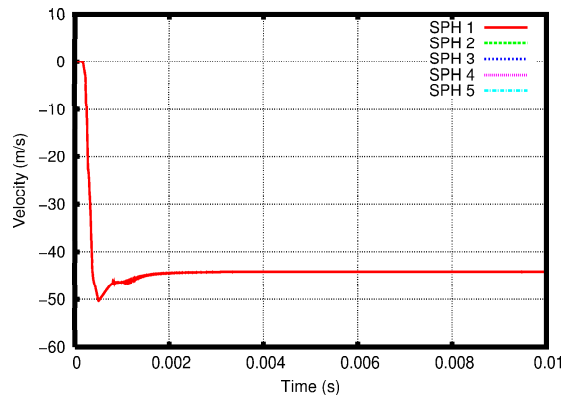


FIGURE 27: Outgoing velocity of the jet (test E20A2)

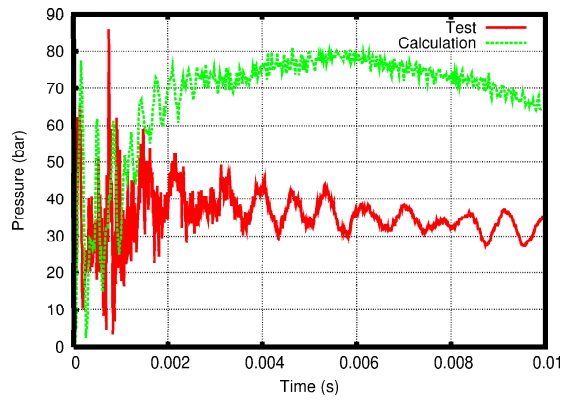


FIGURE 28: The pressure in the cylinder (test FUA5)

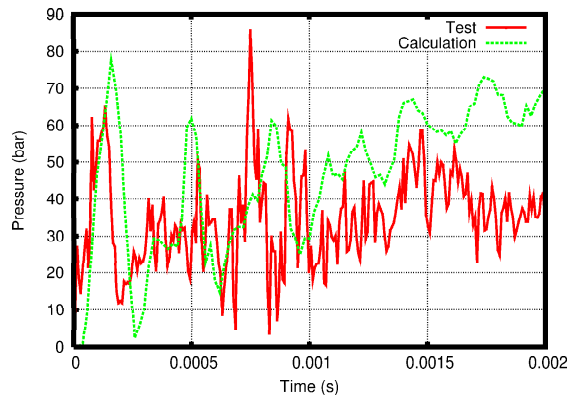


FIGURE 29: The pressure in the cylinder : zoom (test FUA5)

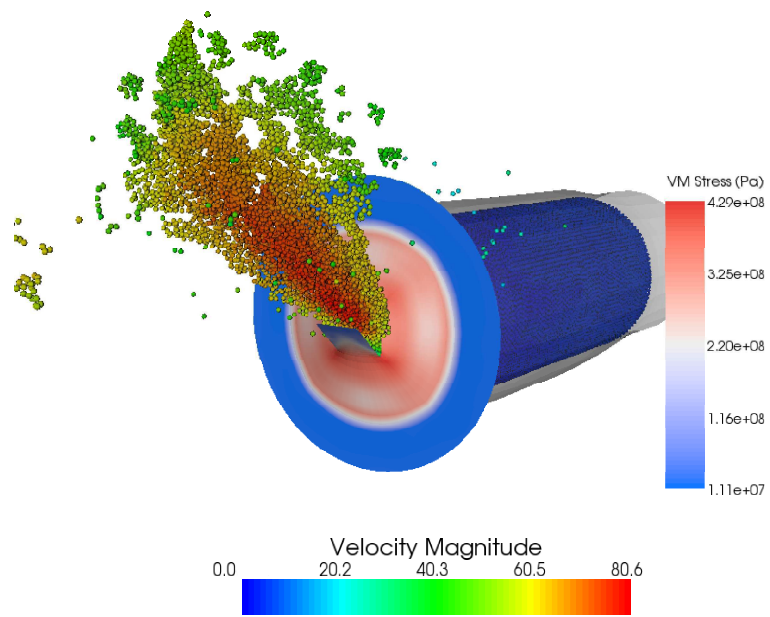
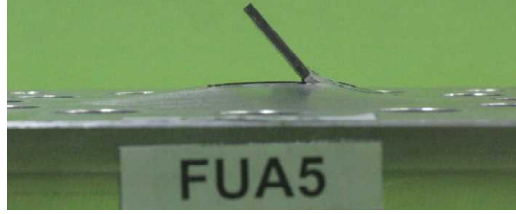
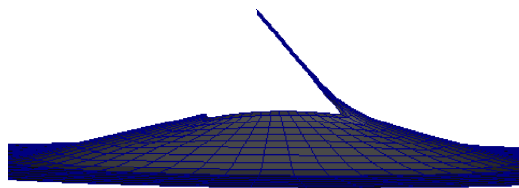


FIGURE 30: The simulation of test FUA5 at $t = 3.5 \text{ ms}$



(a) Experimental deflection, $\alpha \sim 50^\circ$



(b) Numerical deflection at $t = 10 \text{ ms}$, $\alpha \sim 50^\circ$

FIGURE 31: Comparison of the deflections (test FUA5)

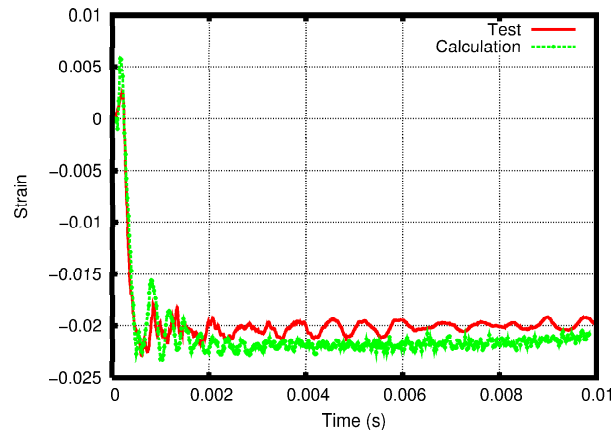


FIGURE 32: Comparison of the strains (test FUA5)

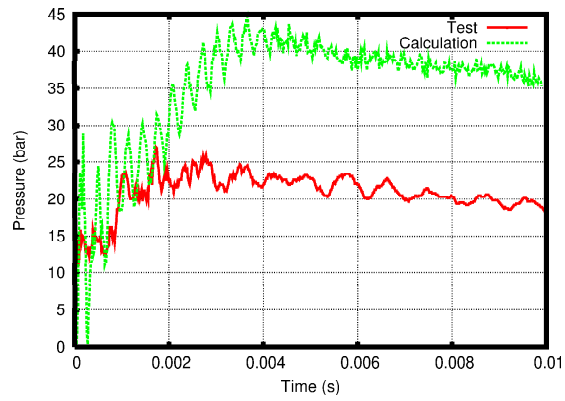


FIGURE 33: The pressure in the cylinder (test FUA2)

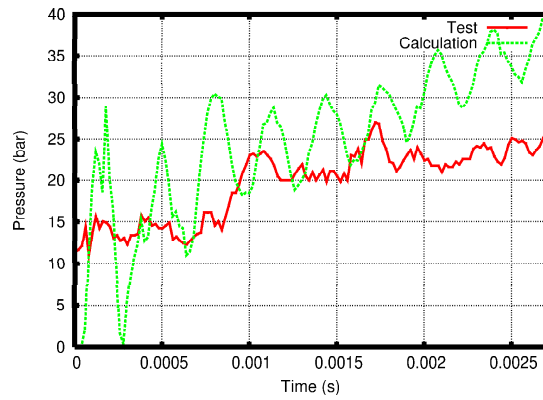
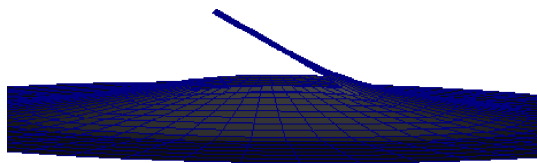


FIGURE 34: The pressure in the cylinder : zoom (test FUA2)



(a) Experimental deflection, $\alpha \sim 20^\circ$



(b) Numerical deflection at $t = 10\text{ ms}$, $\alpha \sim 28^\circ$

FIGURE 35: Comparison of the deflections (test FUA2)

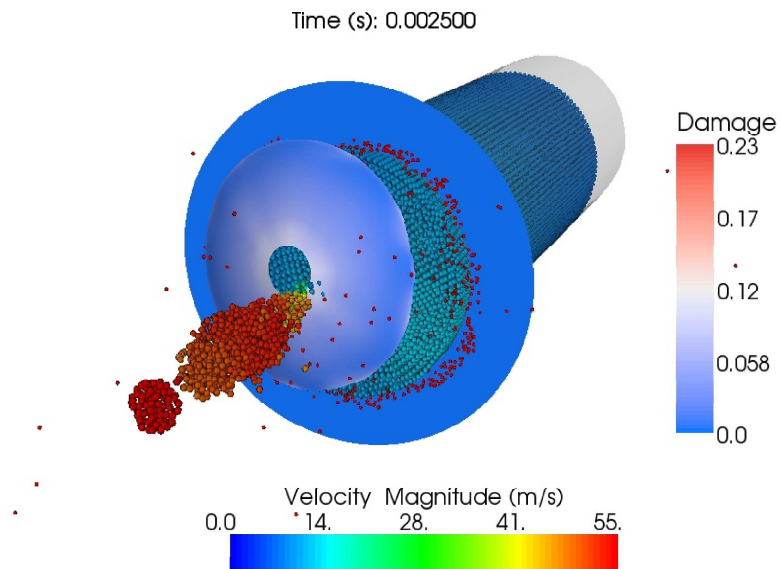


FIGURE 36: The simulation of test TF14A5 at $t = 2.5 \text{ ms}$

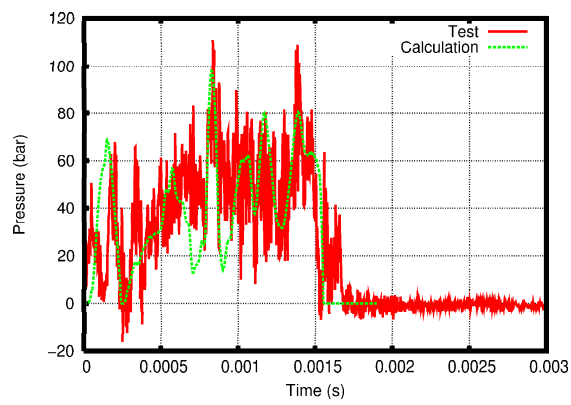


FIGURE 37: The pressure in the cylinder (test TF14A5)

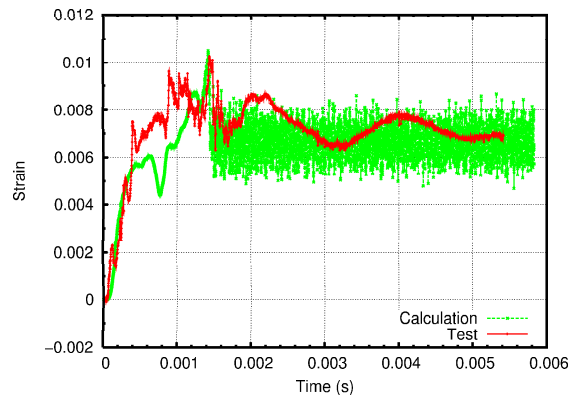


FIGURE 38: The deflection of the specimen (test TF14A5)

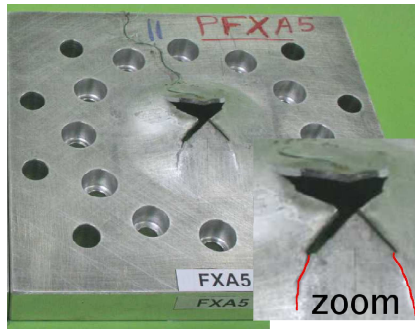


FIGURE 39: Propagation of the cracks (test FXA5)

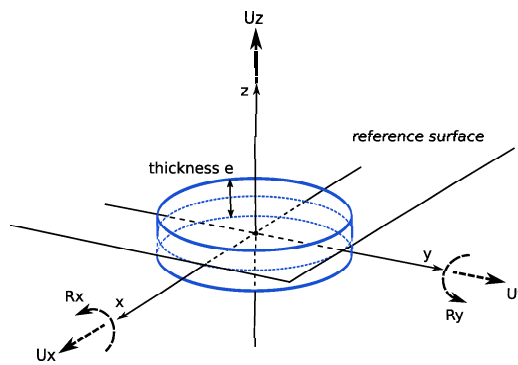


FIGURE 40: An SPHS particle

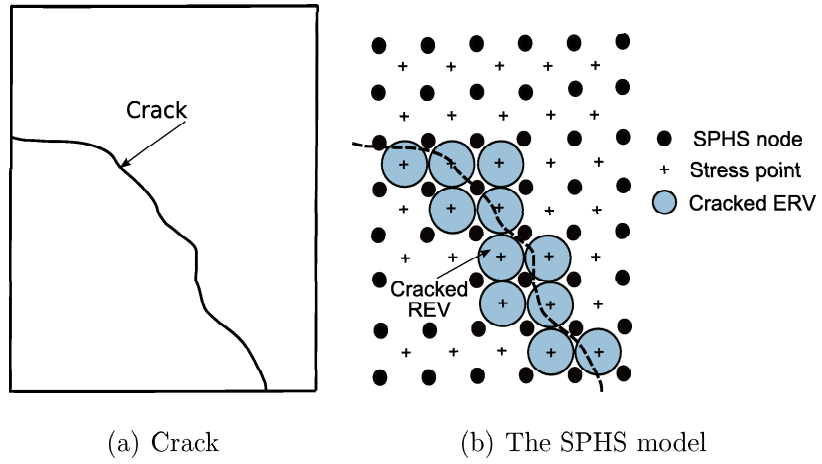


FIGURE 41: Representation of a crack using the SPHS model : example of a regular mesh of quadrilaterals

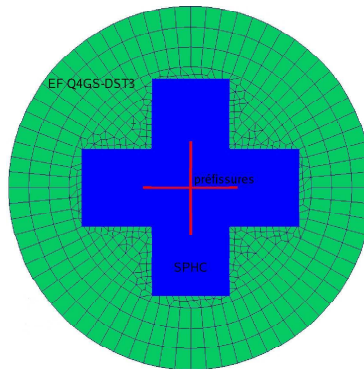


FIGURE 42: The mesh of the specimen (test FXA5)

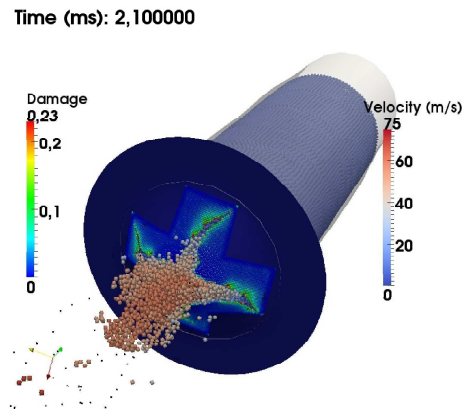


FIGURE 43: The simulation of test FXA5 at $t = 2.1 \text{ ms}$

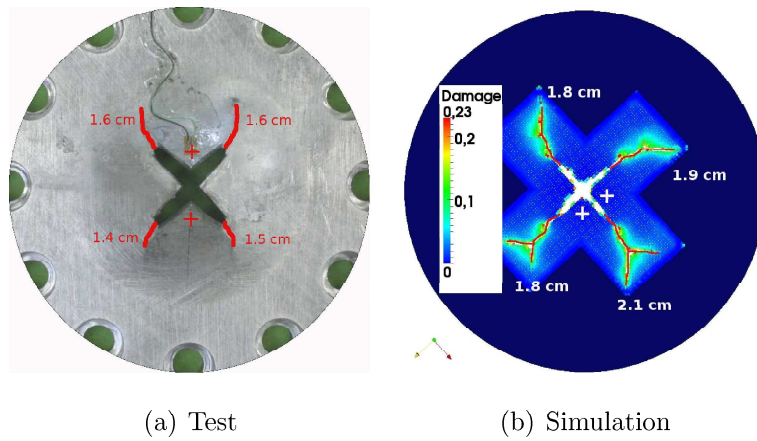


FIGURE 44: Comparison of the paths and lengths of the cracks (test FXA5)

Test	Frequency (Hz)
1-9	$\sim 1,600$
10	$\sim 1,000 - 1,200$
12-13	1,300

TABLE 5: The frequencies observed experimentally

Test number	Characteristics of the specimen			
	specimen	e_p (mm)	Precrack	V (m/s)
1-7	E14A-B-C2 & E14A-B-C-D5	25	hole (d=14mm)	2 & 5
8-9	E20A2 & E20A5	25	hole (d=20mm)	2 & 5
10-11	F14A2 & F14A2-5 ^a	2	hole (d=14mm)	2 & 5
12-13	FUA2 & FUA5	2	U-shaped precrack	2 & 5
14-15	FXA2 & FXA5	2	X-shaped precrack	2 & 5
16	TF14A5	1	hole (d=14mm)	5
17	TFA5	1	no hole	5
18	F14E3A5	2	hole (d=14mm)+ 2 precracks (3mm)	5
19	FE20A5	2	precrack (20mm)	5

TABLE 4: Nomenclature and characteristics of the tests

^a. The same specimen was used for tests 10 and 11.

ϵ_p^s	ϵ_p^c	D_c	$\tau_c(\mu sec)$	a
0.03	0.25	0.23	0.1	2

TABLE 6: The material parameters of the damage law for AU4G 2024 (Suffis, 2004)